Rational design of zeolite Y supported oxalate and borohydride ligands functionalized Cu catalysts for CO$_2$ conversion to specialty chemicals

Olumide Bolarinwa Ayodele [a,b]

[a] Department of Civil and Chemical Engineering, University of Tennesse Chattanooga, 615 McCallie Ave, Chattanooga, TN 37403, United States
[b] School of Chemical Engineering, University of Science Malaysia, Engineering Campus, 14300 Nibong Tebal, Malaysia

ARTICLE INFO

ABSTRACT

This study investigates the effect of oxalate and borohydride ligands functionalization on the properties and activity of zeolite Y (ZY) supported copper nanoparticles in CO$_2$ hydrogenation to specialty chemicals. The ZY-supported copper oxalate (CuX-ZY) and copper borohydride (CuB-ZY) catalysts exhibited a drastic difference in physicochemical properties compared to a benchmark copper supported on ZY (Cu-ZY) catalyst without any functionalization. The average Cu particle sizes are 7.74, 0.69, and 0.57 nm for Cu-ZY, CuX-ZY, and CuB-ZY, respectively. The smaller the copper oxide particle sizes, the higher the reduction temperatures to the metallic state due to strong-metal-support-interactions. The CO$_2$ conversions (X_{CO2}) at 270 °C are 28.3%, 26.4%, and 14.6%, for CuX-ZY, CuB-ZY, and Cu-ZY which aligns with the trend of basic site-strength, Cu particle sizes, and Cu dispersion of the catalysts. While methanol yield was maximum at 70.5 g$_{product}$ g$_{cat}^{-1}$ • min^{-1} over CuX-ZY, the dimethyl ether was maximum at 48.9 g$_{product}$ g$_{cat}^{-1}$ • min^{-1} over CuB-ZY. Furthermore, the oxalate and borohydride functionalization were effective in minimizing CO formation.

1. Introduction

The CO$_2$ hydrogenation to methanol and other specialty chemicals (CHMX) like dimethyl ether (DME) is a challenging process due to the difficulties associated with the activation of CO$_2$ especially increase in the formation of CO at elevated temperatures required for CO$_2$ conversion, and other possible side reactions such as methanation. Therefore, a rational design of efficient catalysts is necessary to improve the overall CHMX process and make it attractive on an industrial scale. Although there has been significant progress in the development of useful catalysts for the CHMX process mostly using promoted Cu metal, the major challenge remains improving the selectivity toward methanol (or other useful oxygenates) by reducing the amount of CO or CH$_4$ formed [1,2]. Metal oxides are frequently used catalyst support to aid the dispersion of the active metals, and the ability of the catalysts to bind and activate CO$_2$ is principally proportional to their basicity and active metal reducibility. Reduced metals oxides are necessary to activate CO$_2$, thus to enhance the catalyst surface chemistry and activity for CO$_2$ activation, the reduced state of the metal must be maintained throughout the reaction time [1]. Presently, Cu/ZnO/Al$_2$O$_3$ is the state-of-the-art industrial catalyst, wherein Cu is the main active site while ZnO plays the role of a physical spacer to isolate Cu nanoparticles (NPs) and achieve

high Cu dispersion to provide a high number of Cu active sites for CO$_2$ hydrogenation [3,4]. Albeit, the Cu-ZnO synergy effect has shown a positive contribution to the CO$_2$ hydrogenation activity, whilst excess ZnO covered the active Cu sites with a negative effect on the catalytic activity [3,4].

Highly dispersed accessible Cu active sites are an important key to the high performance of the CuO/ZnO/Al$_2$O$_3$ catalyst system with a linear relationship between activity and Cu surface area among samples prepared via the same protocol [5]. However, between these families considerably different intrinsic activities normalized by the Cu surface area can be found which showed that methanol synthesis over Cu appears also to be a structure-sensitive reaction [5,6]. Thus, different "qualities" of Cu surfaces with different interactions with supports have been prepared that vary in the activity of their active sites and/or in the concentration of these sites [3]. For example, Witoon et al.[7] showed that there is a strong structure-activity relationship for amorphous (a-), tetragonal (t-), monoclinic (m-) ZrO$_2$ phase supported copper catalysts for methanol synthesis from CO$_2$ hydrogenation. The order of copper surface area was found to be Cu/a-ZrO$_2$ > Cu/t-ZrO$_2$ > Cu/m-ZrO$_2$ which correlated with the increased yield of methanol. However, normalization of the copper site-specific activity which was measured in terms of turnover frequency for methanol (TOF$_{methanol}$) over Cu/t-ZrO$_2$

ranged from 1.10 to 1.50 times and 1.62–3.59 times higher than over Cu/a-ZrO$_2$ and Cu/m-ZrO$_2$, respectively. The high TOF$_{methanol}$ over Cu/t-ZrO$_2$ was ascribed to a strong Cu–ZrO$_2$ interaction which was validated by the X-ray absorption spectroscopy (XAS). According to their x-ray absorption near edge structure (XANES) spectra for the catalysts, Cu/m-ZrO$_2$ catalyst demonstrated obvious absorption edge at 8983 eV, indicating that the chemical environment of copper species in Cu/m-ZrO$_2$ catalyst resemble CuO reference material which its local structure was square-planar coordination geometry. For the Cu/t-ZrO$_2$ and Cu/a-ZrO$_2$ catalysts, the absorption edge shifted higher to 8984.6 and 8985.6 eV, respectively, suggesting a change of the geometric coordination of copper sites from square-planar to octahedral structure. The authors maintained that this observation indicated that there is a strong interaction between copper oxide species and the ZrO$_2$ supports in both Cu/t-ZrO$_2$ and Cu/a-ZrO$_2$ catalysts. This trend was consistent with their TPR result which showed CuO species reduction peaks at 202, 209, and 232 °C for Cu/m-ZrO$_2$, Cu/a-ZrO$_2$, and Cu/t-ZrO$_2$ catalysts, respectively.

Generally, in supported metal catalyst only the atoms on the surface of the nanoparticle or nanoclusters act as the active sites, while those inside the nanoparticles/clusters acts as mere spectators, i.e., not participating in the reaction, thus leading to a waste of the active metals. Therefore, the specific activity per metal atom usually increases with decreasing the metal particles size, thereby making metal particles size a key factor in determining the performance and stability of catalysts [8, 9]. In fact, the electronic properties, catalytic activity, and even the optical properties of nanomaterials are strongly influenced by their size (and also shape and structure) in complex ways that are very difficult to predict [10]. Furthermore, the lower the metal particle size the better the degree of metal dispersion which is responsible for boosting the catalytic efficiency. Although, it is well known that the surface free energy of metals increases significantly with decreasing particle size, thereby promoting aggregation of small clusters [9]. This challenge can be safely mitigated using appropriate support material that strongly interacts with the downsized metal species to prevent aggregation, thus creating stable, finely dispersed metal atoms (clusters) with high catalytic activity [9,11,12]. A facile strategy is through ion-exchanged metals supported on porous materials such as metal-organic frameworks (MOFs) and zeolites, as well as organometallic complexes anchored unto a support [9]. Another challenge to supported metal catalysts is the inhomogeneous wide range of metal sizes from nanoparticles to subnanometer clusters which do not only reduces the metal-atom-efficiency but also frequently leads to undesired side reactions since broad size distributions of active metal and irregular morphology of each metal particle may favor different selectivity. One reliable route to downsize metal particle size towards achieving homogeneous (or at least, near-homogeneous) particle sizes and narrow particle size distribution is the application of surface organometallic chemistry (SOMC) which has emerged as a powerful approach to generate single-site catalysts [13–16]. To achieve this, functionalization of the Cu precursors with sodium borohydride (NaBH$_4$) and organic ligands such as oxalate quickly comes to the fore. These techniques have been reported to guarantee very small active metal particle sizes, chemo-reduction of the metal oxidation states, and very high active metal dispersion. The reports on the functionalization of Cu/ZnO precursors with oxalate ligands (OxL) [17–19] and co-impregnation of HAuCl$_4$ and Cu(NO$_3$)$_2$ with NaBH$_4$ solution (SBH) [20], and M-promoted (M = Cr, Zr, and Th) Cu modified with SBH showed that the metal nanoparticles exhibited smaller particles sizes, higher dispersion, and stability of the resulting catalysts leading to higher activity and selectivity [19–21]. Thus, synthesizing unpromoted Cu with OxL and SBH functionalization supported on zeolitic materials is a promising and interesting adventure especially due to the zeolites shape-selective catalysis. For example, HZSM-5 zeolite is selective towards DME and gasoline, whereas SAPO molecular sieves are preferred for light olefin generation, i.e., SAPO zeolite windows allowed only small linear hydrocarbons to pass through, while H-ZSM zeolite windows allowed much larger branched and linear hydrocarbons [22]. Although, the structure-property relations between zeolite properties and CO$_2$ hydrogenation into different oxygenates have not yet been systematically investigated [22].

As earlier mentioned, there is a common consensus that the Cu active site is responsible for the CO$_2$ hydrogenation to methanol and other specialty chemicals [1]. Thus, to gain a thorough understanding in the continuous search for the best Cu sites, structure, and electronic properties, investigations should be conducted in the absence of ZnO to avoid its interference with both the Cu electronic and structural properties. More so that the presence of ZnO increases the intrinsic activity of Cu-based catalysts due to the Cu-ZnO synergy [3]. This has generated several different and sometimes contradictory mechanistic models [3], which are largely due to the ZnO nanocrystals undergoing dynamic change caused by both adsorbate-induced changes in surface energies and by the changes in the interfacial energy [23]. Therefore, it is interesting to improvise a facile synthesis protocol for supported Cu nanoparticles to maintain structural stability with high dispersion even without the ZnO. So far from the literature, application of either oxalate ligands or NaBH$_4$ solution to functionalize only Cu precursor to synthesize highly dispersed very small Cu particle sizes strongly interacting with the support for CO$_2$ reduction to methanol and other specialty chemicals like DME has not been sighted by the author. Thus, this study investigated the applicability and influence of oxalate ligand (OxL) functionalization using oxalic acid and sodium borohydride modification at the synthesis stage of copper nanoparticles supported on zeolite Y (ZY) for CO$_2$ reduction to oxygenates, specifically methanol and DME. The choice of zeolite Y was due to its combined large surface area (>1500 m2/g), high Si/Al ratios, excellent open-framework structures with a supercage cavity size of ~11.24 Å, easily tunable pore structure, and more importantly good hydrothermal stability which has qualified ZY as fluidized catalytic cracking catalytic material in petroleum refining industry [24,25]. The synthesized ZY supported functionalized Cu nanoparticles were carefully tailored to meet the expected properties of typical CO$_2$ hydrogenation to oxygenates catalysts such as enhanced copper surface area which is the main factor that controls the yields of products, strong Cu–support interaction to improve the spillover of atomic hydrogen from the copper surface, and strong basic site to increase the adsorptive capacity of CO$_2$ for H$_2$ reduction at the active sites. Furthermore, the properties (structural and electronic) of the catalysts and activity were correlated and compared with a conventional Cu/ZY catalyst, i.e., without OxL or SBH functionalization. The OxL functionalized catalyst exhibited instances of copper carbide (Cu-C) which favored high methanol yield, while the SBH functionalized catalyst favored DME due to increased acidity from instances of copper boride (Cu-B) sites.

2. Experimental

2.1. Materials and methods

Copper nitrate trihydrate (Mwt: 241.6 g/mol, $\geq$ 99.0%) and sodium borohydride (NaBH$_4$) were purchased from Sigma Aldrich, while zeolite Y (ZY) used as the catalyst support and oxalic acid were purchased from Spectrum chemicals. All the materials were used without any pretreatment.

2.2. Catalyst synthesis

Three different Cu supported on ZY were synthesized with a Cu loading of 2% (wt/wt). The first catalyst was without any ligand functionalization by adding the predetermined amount of copper nitrate trihydrate solution to ZY dispersion and stirred for 6 h at 60 °C to ensure incorporation of Cu into the ZY matrix and exchange with intergallery aluminum. The second and third catalysts were synthesized in a two-
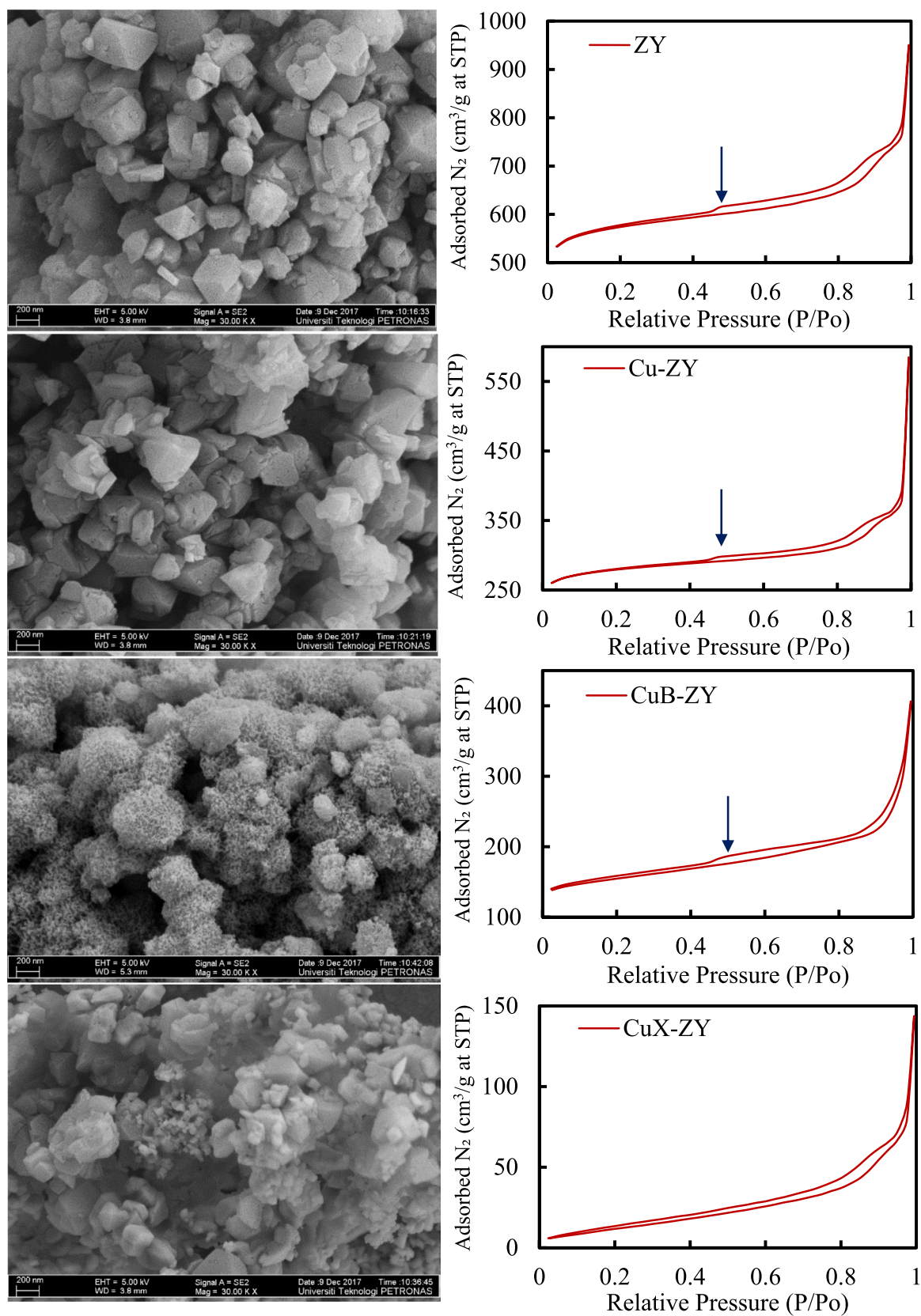
Fig. 1. FESEM, N$_2$ adsorption-desorption isotherms of ZY, Cu-ZY, CuB-ZY, and CuX-ZY catalysts.

step protocol; firstly by reacting copper nitrate trihydrate with either oxalic acid or NaBH$_4$ to produce copper oxalate and copper borohydride complex ligands which were subsequently added to ZY dispersion at 60 ºC and stirred for 6 h. For all the samples, the stirring continues for another 2 h without heating to allow the colloidal suspension to cool down before filtration and washing with anhydrous ethanol. The samples were dried in the oven at 120 ºC overnight and calcined at 360 ºC for 4 h with a slow temperature ramping of 4 °C/min. The calcination temperature and the slow heating rate were carefully chosen since calcination above 400 ºC and higher heating rates initiate agglomeration of active metals, dealumination of framework aluminum, and shrinking of the zeolite pore structures [26]. With this safe thermal treatment, any observed variation in the structural, electronic, and textural properties of the functionalized catalysts can be conveniently ascribed to the effects of OxL and SBH functionalizations. The first copper supported on ZY catalyst without any ligand functionalization was designated Cu-ZY, while the oxalate ligand and borohydride functionalized catalysts are denoted CuX-ZY and CuB-ZY, respectively.

2.3. Catalyst characterization

Extreme high-resolution field emission scanning electron microscope (XHR-FESEM) and energy dispersive X-ray (EDX) were performed to determine the samples morphology and elemental composition, respectively using Verios XHR-FESEM (Model 460 L, FEI™) equipped with an EDS detector. Nitrogen adsorption-desorption measurements (BET method) were performed at liquid nitrogen temperature (-196 ℃) with an autosorb BET apparatus, Micromeritics ASAP 2020, surface area and porosity analyzer to determine the surface area, pore size and structure, and the pore volume. The catalyst microstructure and crystallographic information were studied by high-resolution transmission electron microscope (HRTEM) 200 kV with Field Emission (TECNAI G2 20 S-TWIN, FEI™). The crystalline structure of the catalyst was determined by X-ray diffraction (XRD) recorded on a powder diffractometer (Philips X′ Pert MPD, 3 kW) using Cu Kα radiation (λ = 1.5405 Å). Fourier Transformed Infrared Spectroscopy (FTIR) analysis was performed on the ZY support and the synthesized ZY supported catalyst using a Perkin-Elmer Spectrum GX Infrared Spectrometer with a resolution of 4 cm^{-1}, in the range of 4000 – 450 cm^{-1} to determine their surface functional groups, presence and extent of Bronsted acidic character and inherent acidity. Hydrogen temperature-programmed reduction/desorption (H$_2$-TPRD) was performed on the catalysts to study their reduction behavior using a Thermo Finnigan TPD/R/O 1100 equipped with a thermal conductivity detector and a mass spectrometer. Typically, 20 mg catalyst was placed in the U-shaped quartz tube. Catalyst samples were degassed under a flow of nitrogen at 200 °C to remove traces of water and impurities from the catalyst pores. H$_2$-TPRD was performed using 5% H$_2$/N$_2$ with a flow rate of 20 ml/min and heating from 40° to 900°C at 5 °C/min. The amount of surface metallic copper in moles, n_{Cu}, the exposed Cu surface area, S_{Cu}, were calculated according to Eqs. 1–2. Electron spectroscopy for chemical analysis (ESCA) was carried out using X-ray photoelectron spectroscopy (XPS - Thermo-Fischer K-Alpha) to obtain the chemical nature, surface composition, oxidation state, relative surface compositions, and the type of interaction between the Cu metal and the ZY support. The XPS was equipped with a monochromatized AlKα source and the resulting spectra from the samples were analyzed using the Avantage software for peak fitting and identification of chemical state. The basicity and acidity tests were carried out using temperature-programmed desorption (TPD-CO$_2$ and TPD-NH$_3$, respectively) using Thermo Finnigan (model TPDRO 1100 series) instrument. The sample was pretreated under the flow of N$_2$ gas (30 ml/min) at 150 °C for 40 min, followed by adsorption with CO$_2$ (NH$_3$) gas for 60 min at room condition. The excess of CO$_2$ (NH$_3$) was subsequently flushed out by flowing N$_2$ gas before the analysis. The desorption of the CO$_2$ (NH$_3$) from the basic/acid sites of the catalyst was identified by TCD under helium gas (30 ml/min) ranging from 50 ℃ to

900 ℃ at a heating rate of 10 ℃ min^{-1}.

$$n_{Cu} = 2 \times n_{H2} \tag{1}$$

$$S_{Cu} = (n_{Cu} \times N)/(1.4 \times 10^{19} \times W)(m^2\ g^{-1}) \tag{2}$$

where n_{H2} is the amount (in moles) of hydrogen consumed, N is Avogadro's constant (6.02×10^{23} atoms mol^{-1}), 1.4×10^{19} is the number of copper atoms per square meter, and W is the weight of the catalyst [20].

2.4. Catalytic activity measurements

The detailed activity measurement procedure has been previously reported [17,18]. Briefly, the CO$_2$ hydrogenation reaction was performed in a fixed-bed microreactor (PID Eng & Tech). In a typical experiment, 20 mg of the synthesized catalyst (Cu-ZY, CuX-ZY, or CuB-ZY) whose activity is to be studied was sandwiched between quartz wools to ensure an isothermal temperature zone around the catalyst and gently loaded into a stainless-steel tube reactor. Before the reaction, the calcined Cu-ZY, CuX-ZY, and CuB-ZY were reduced in situ using 20 ml min^{-1} of 5% H$_2$ in He for 4 h under atmospheric pressure at 470, 550, and 570 ℃, respectively based on the H$_2$-TPR result. After the reduction step, a feed consisting of a mixture of H$_2$ (54 ml/min) and CO$_2$ (18 ml/min) was fed to the reactor and the reaction was performed within a temperature range of 180 – 270 °C at 2.25 MPa for a total 10 h time-on-stream (TOS). All post-reactor lines and valves were heated to 180 °C to prevent condensation. The feed and gaseous products were analyzed by an on-line gas chromatograph (Agilent 7890 A) equipped with two TCD detectors as well as HayesepQ and molsieve columns for analyses of H$_2$ and permanent gases. Methanol, DME other hydrocarbons were analyzed using a DB-1 column and an FID detector. CO$_2$ conversion, reaction products selectivity, and space-time yield (g$_{product}$ g$_{cat}^{-1}$ • min^{-1}) of respective products are defined as follows (Eqs. 3–5):

$$CO_2\ conversion = \frac{moles\ of\ CO_{2_{in}} -\ moles\ of\ CO_{2_{out}}}{moles\ of\ CO_{2_{in}}} \tag{3}$$

$$\%S_i = \frac{p_i}{\sum_{i=1}^{p} products} * 100 \tag{4}$$

$$Space-time\ yield\ (STY) = \frac{P_i}{moles\ of\ CO_{2_{in}} * amount\ of\ catalyst * MV} * MW_i * V_{CO_2} \tag{5}$$

where P_i and MW_i are the moles and molecular weight (g mol^{-1}) of respective product observed, while V_{CO_2} and MV are the volumetric flow of CO$_2$ (cm^3 min^{-1}) and molar volume of an ideal gas (22,400 cm^3 mol^{-1}), respectively and $_{Si}$ is the selectivity of each product species.

3. Results and discussions

3.1. Characterization results
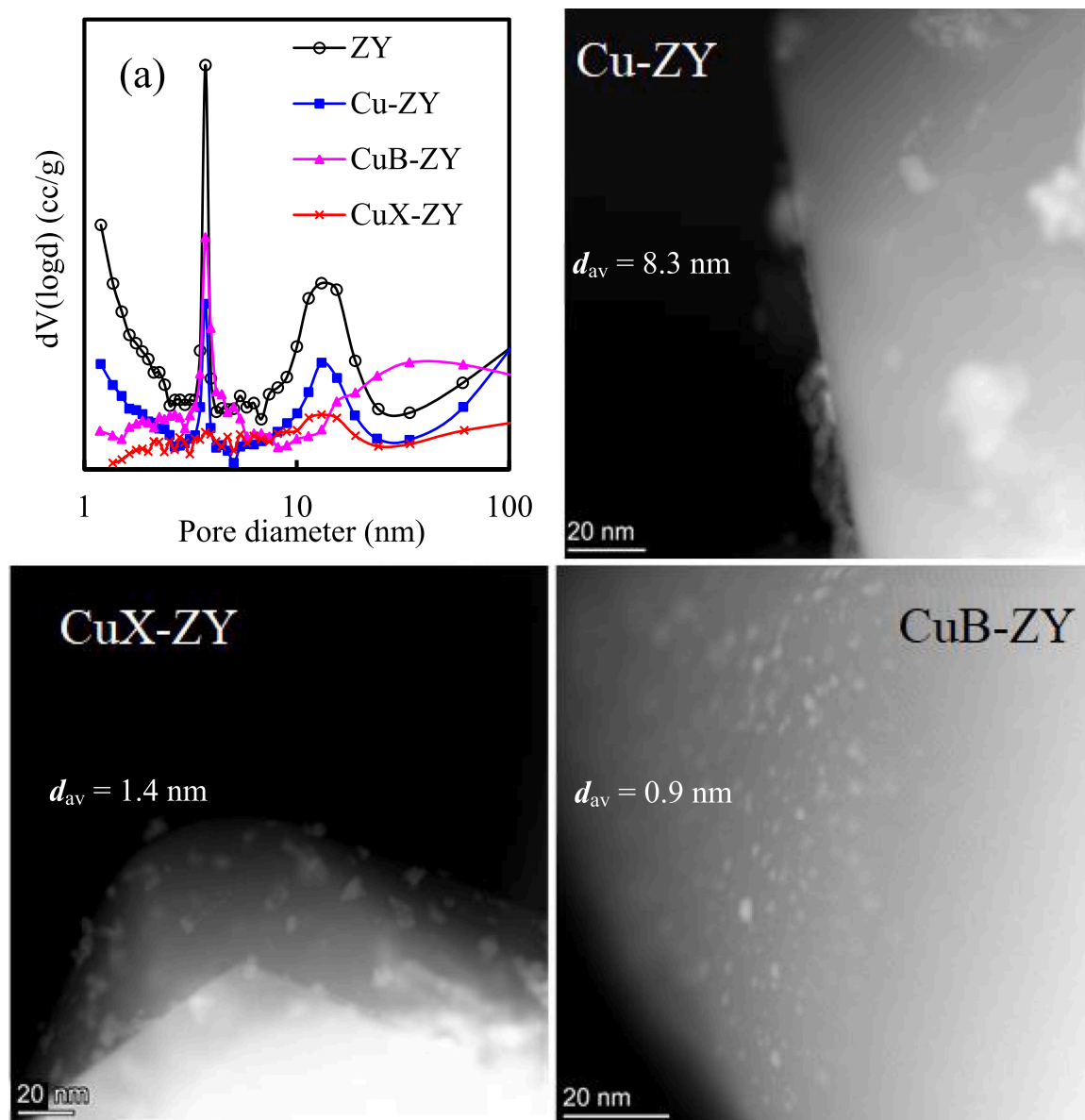
3.1.1. Morphology and textural properties

The morphologies of the ZY, Cu-ZY, CuX-ZY, and CuB-ZY shown in the first row of Fig. 1 reveal the extent of morphological variations in the samples due to incorporation of Cu, and impacts of the oxalate ligand and sodium borohydride functionalizations. There is no significant variation in the morphology of Cu-ZY compared to that of the ZY support. However, when the CuB precursor was incorporated into ZY, the morphology of the CuB-ZY transforms completely due to the borohydride functionalization leading to a spongy structure with increased porosity which may be ascribed to the voids created by the escaping H$_2$ gas during synthesis (Eq. 6) [27]. Similarly, with the incorporation of

Table 1

Textural properties of ZY, Cu-ZY, CuB-ZY, and CuX-ZY.

	Micropore volume (cm³/g)	Mesopore volume (cm³/g)	Total volume (cm³/g)	Av. Pore diameter (nm)	Micropore area (m²/g)	External surface area (m²/g)	BET Surface area (m²/g)
ZY	0.77	0.01	0.78	1.2	1523	220	1743
Cu-ZY	0.34	0.23	0.57	2.12	733	137	870
CuB-ZY	0.14	0.33	0.47	3.72	323	162	484
CuX-ZY	0.00	0.24	0.24	1.19	0	102	102

Av. = Average.

Fig. 2. Pore structure of ZY, Cu-ZY, CuB-ZY, and CuX-ZY samples and the STEM-HAADF image of Cu-ZY, CuB-ZY, and CuX-ZY catalysts.

the CuX precursor into ZY there is an obvious reduction in the ZY size and crystallinity. Previous studies on OxA ligand functionalization of active metals (Co and Ni) supported on different aluminosilicate materials (zeolites and clay minerals) [8,15,28] also showed varying degrees of crystallinity loss due to OxA acidity which consequently led to the removal of extra-framework alumina.

$$Cu(NO_3)_2 + 2NaBH_4 + 3H_2O \rightarrow 0\cdot5Cu_2B + 2NaNO_3 + 1\cdot5HBO_2 + 6\cdot25H_2 \quad (6)$$
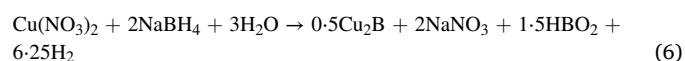
The second column of Fig. 1 showed the isotherms of the ZY support and the synthesized catalysts which according to IUPAC classification corresponds to the Type IV isotherms, i.e., they are characterized by the hysteresis loop that is associated with capillary condensation taking place in mesopores. The hysteresis loop of ZY, Cu-ZY, and CuB-ZY conforms to the H3 hysteresis which shows the presence of non-rigid
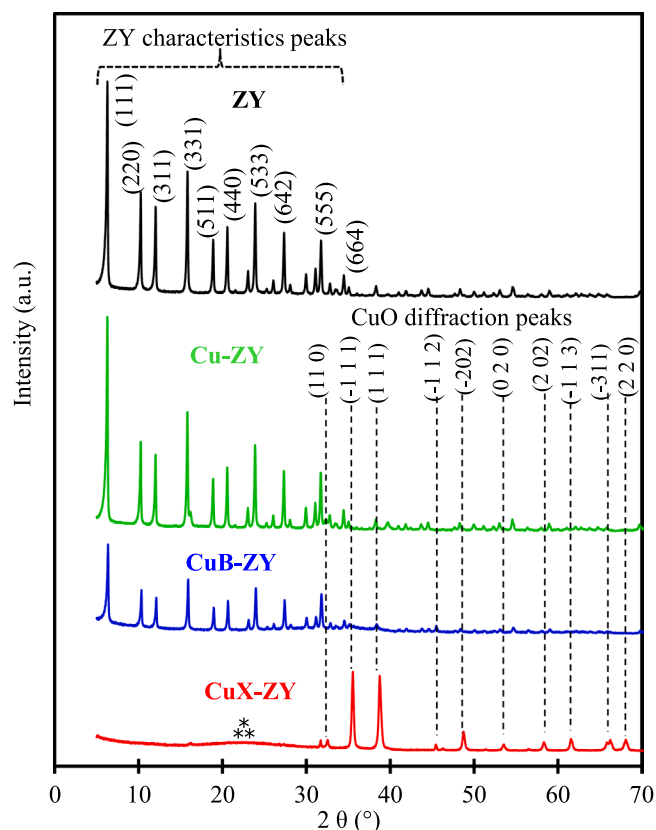
Fig. 3. X-ray diffraction patterns of ZY, Cu-ZY, CuB-ZY, and CuX-ZY.

Fig. 4. FTIR spectra of ZY, Cu-ZY, CuB-ZY, and CuX-ZY.

aggregates of plate-like particles, i.e., slit-shaped pores. The multilayer film point where the desorption isotherm meets the adsorption isotherm at $P/P_o \approx 0.45$ in ZY, Cu-ZY, and CuB-ZY samples (downward blue arrow) disappeared in CuX-ZY and its hysteresis loop systematically matched the H4 configuration which indicates narrow slit pores (including pores in the micropore region). The variation in the hysteresis loop is in agreement with the earlier observation which showed that the wider the pore size distribution the less sharp is the pore condensation step [29]. This is supported by the textural properties in Table 1 which showed that the ZY has higher microporous components (approximately 98.7% micropore volume and 87.4% micropore area). The trend of higher microporous components is still reasonably preserved in the Cu-ZY with approximately 60% micropore volume and the 84.3% micropore area. However, the trend was reversed in the CuB-ZY and CuX-ZY samples, while the former has 29.8% micropore volume, the latter showed zero microporous structure. Furthermore, the total volume also reduced following the trend ZY > Cu-ZY > CuB-ZY > CuX-ZY. This trend can be evidently seen in the pore structure Fig. 2 (row 3 of column 1) which confirms the gradual reduction in the micropore volume of Cu-ZY and CuB-ZY, and total disappearance in CuX-ZY. A reverse trend is seen in the mesopore pore volume, especially with CuB-ZY that showed a well-developed mesopore pore volume and enhanced pore diameter, ostensibly arising from the hydrogen gas evolution (Eq. 6). This phenomenon showed that beyond morphological variations earlier seen, both the OxA and SBH functionalization were impactful on the textural properties. The drastic reduction and disappearance in the micropore structures of the CuB-ZY and CuX-ZY samples are due to the blocking of the pores with nano and sub-nano CuO particles, respectively.

According to the average particle size of the CuO particles in the HRTEM images, the Cu-ZY, CuX-ZY, and CuB-ZY samples exhibited average particle sizes of 8.3, 1.4, and 0.9 nm, respectively, i.e., the Cu mean particle diameter followed Cu-ZY >> CuX-ZY > CuB-ZY. In
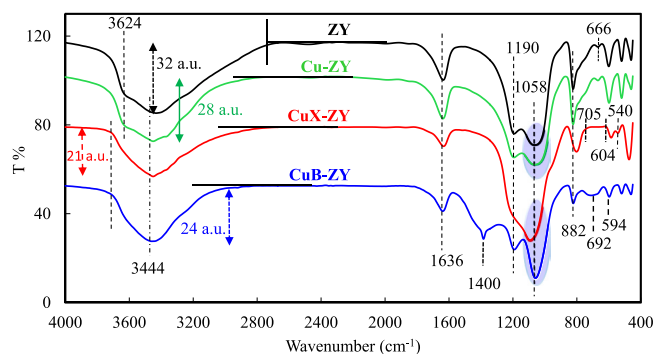
previous studies [17,30] on CuZnO supported on ZSM-5, the sample having a lower average metal size of 2.4 nm showed noticeable 4.11% and 34.56% reduction in the micropore area and external surface area, respectively, and the reductions were ascribed to blocking of the pores by the metal oxide nanoparticles. On the other hand, the catalyst having larger average particles sizes of 8–15 nm does not show any reduction, instead, an increase in those properties was observed which were ascribed to the protonation effect of OxA functionalization. The obvious transformation in the morphology of CuB-ZY to spongy outlook with an increase in pores could be responsible for the increase in the pore diameter in Fig. 2.

3.1.2. Structural properties

The XRD patterns for the ZY support in Fig. 3 revealed strong zeolite Y characteristics diffraction peaks at $2\theta = 6.2, 10.2, 12.1, 15.8, 18.9, 20.5, 23.9, 27.4, 31.6, 31.8, 33.4$ and $34.5°$ that are indexed to (111), (220), (311), (331), (511), (440), (533), (642), (822), (555), (840), (664) planes, respectively [31]. Upon the incorporation of the Cu precursors, the synthesized catalyst showed different extents of dramatic variations in their respective diffraction patterns. Both Cu-ZY and CuB-ZY showed loss of intensity in those characteristics ZY peaks, while the loss was marginal in the former, it was significantly pronounced in the latter which was ascribed to the effects of the SBH modification. However, there was a complete loss of crystallinity in the CuX-ZY sample turning it amorphous due to the protonic effect from the oxalic acid that was used for the functionalization. According to previous studies [12, 32–34], it has been sufficiently demonstrated that zeolite and other aluminosilicates minerals like kaolinite undergo loss of extra framework alumina under acid treatment which usually leads to loss of crystallinity. The extent of extra framework alumina loss which resulted in crystallinity loss is dependent on the acid concentration, agitation speed, leaching time, and temperature, as well as the Si-O-Al bonding strength of the aluminosilicate mineral. The diffraction peaks of CuO are not distinctively visible in the Cu-ZY and CuB-ZY due to the overshadowing by the highly intense ZY peaks, especially in the Cu-ZY sample, and high dispersion arising from finely downsized CuO nanoparticles to sub-nanoclusters in CuB-ZY as it will be further shown in subsequent sections. The disappearance of the ZY sharp peaks in the CuX-ZY sample gave way to the reflection of highly crystalline CuO diffraction peaks nanoparticles at $2\theta = 32.5, 35.5, 38.6, 46.3, 48.9, 53.4, 58.2, 61.5, 66.3,$ and $68.0°$ [35]. The broad amorphous diffraction peak at $2\theta = 22.9°$ ($\ast\ast$) was ascribed to the remnant of decomposition of $CuC_2O_4 \cdot xH_2O$ during calcination [21]. The XRD patterns clearly showed that the samples preparation protocols employing OxA and SBH functionalization has effects on the structural information and it is in tandem with previous reports where the type of catalyst precursors and the solvent used (deionized water, DMF, ethanol, and diethylene glycol) during preparation significantly impacted the structural integrity of the resulting catalysts [19,36].

Table 2

NH$_3$-TPD profile to determine the acid strengths and acid densities of Cu-ZY, CuX-ZY, and CuB-ZY catalyst.

	Cu-ZY	CuX-ZY	CuB-ZY
Desorption temperature (°C)	234	372	438
Amount gas adsorbed (μmol/g)	24,774.68	1650.72	4548.72
Acid site (m^2/g$_{catalyst}$)	693.76	46.23	178.05

3.1.3. FTIR and surface acidity (NH$_3$-TPD)

To further understand the impact of the OxA and SBH functionalization on the surface chemistry of the catalysts, FTIR analysis was performed and the result is shown in Fig. 4. From the ZY spectrum, the typical zeolitic broad band with a center around 3444 cm^{-1} which has been assigned to structural OH functional groups with considerable acidity and bridging OH-groups (such as $\equiv$Al (OH) Si$\equiv$ groups with Bronsted acidic character) [37] can be seen up to the stretched region at 3624 cm^{-1}. The band at 3444 cm^{-1} reduced in both intensity and broadness in all the catalysts with CuX-ZY and CuB-ZY exhibiting the highest reduction, while the more acidic hydroxyl band 3624 cm^{-1} also completely disappeared in these samples. Furthermore, the terminal Si-OH groups with inherent acidity at 882 cm^{-1} reduced significantly in the functionalized samples which is an indication of considerable loss of acid sites. The −OH groups on the zeolite surface are important since they may become active centers, e.g., in acid-base catalytic reactions, or adsorption centers during the formation of adsorption complexes [38]. This observation is further corroborated by the NH$_3$-TPD study for the surface acidity of the samples shown in Figure S1 and quantified in Table 2. According to Figure S1, the main NH$_3$ desorption peaks for the Cu-ZY, CuX-ZY, and CuB-ZY catalyst are 234, 372, 438 °C which are attributed to the weak, intermediate, and strong acid strengths, respectively [17]. The weak acid sites are ascribed to the Brønsted acid sites at surface hydroxyls from the zeolitic material framework and weak Lewis acid sites due to the presence of incorporated metal species, while the intermediate acid strength is due to a higher degree of metal oxide (i.e., CuO) downsizing with a metal dispersion, and the strong acid strength peak was ascribed to the strong acid site within the pores of the catalyst [18] (see FESEM of CuB/ZY in Fig. 1, increased pore structure for CuB/ZY Fig. 2a and Table 1). On the other hand, the acid site density followed the trend Cu-ZY > > CuB-ZY > CuX-ZY.

The band around 1190 cm^{-1} is ascribed to pore opening vibrations [37], the band disappeared in CuX-ZY which is in agreement with the loss of micropore structures in CuX-ZY catalyst according to the textural properties in Table 1 and pore structures plot in Fig. 2. In contrast, the band slightly increased in CuB-ZY which also confirms the marginal enhancement of the CuB-ZY textural properties in Table 1. The absorption band at 1636 cm^{-1} is due to the bending mode of vibration of water molecule [35], the band reduced in the CuB/ZY and CuX-ZY as a result of significant loss of physisorbed water during calcination which agrees with the variation in their textural properties and the XRD results. The flattening of the band between 705 and 604 cm^{-1} in the CuX-ZY confirmed significant instances of extra framework dealumination from the Si-O-Al structure (of peak 666 cm^{-1} in ZY) due to the protonation effect from the oxalic acid [12]. The CuB-ZY spectrum showed additional special borohydride features. Typical metal (M)-hydrogen-boride bridge, ν(M-H$_b$-B), has been reported in the range 1300–1500 cm^{-1} [39], and the M-B and M-B-O bonds have been assigned to peaks at ~1392 cm^{-1} and ~1338 cm^{-1}, respectively [40]. Thus, the overlapping bands with a peak at 1400 cm^{-1} in CuB/ZY sample were assigned to the overlapping of Cu-B with either Cu-H$_b$-B or Cu-B-O. The minuscule broad band with minima at 692 cm^{-1} could be due to the overlapping of typical B—O bonds (690 cm^{-1}) and M—O bonds (734 cm^{-1}) [39].

Infrared spectroscopy can reflect the change of the framework configuration of the ZY host after the incorporation of the active metal, i. e., Cu. The FTIR spectra of the Cu samples showed a series of distortion
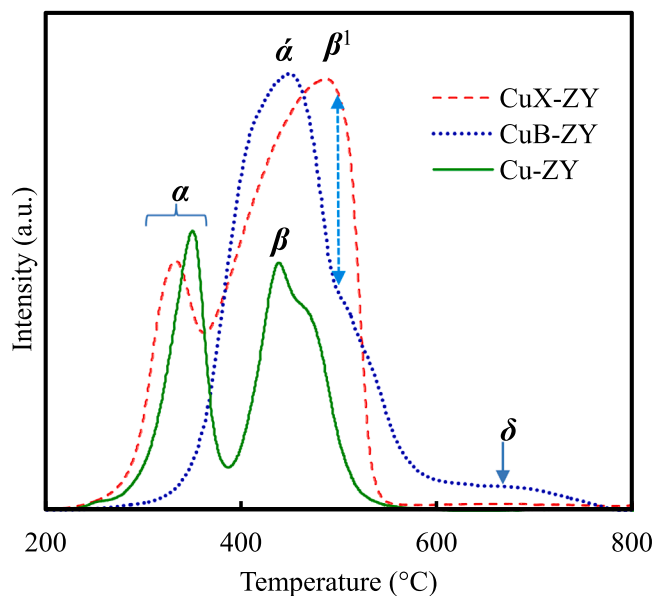

Fig. 5. TPR profile of Cu-ZY, CuB-ZY, and CuX-ZY sample.

Table 3

H$_2$ Temperature-programmed reduction data of Cu-ZY, CuB-ZY, and CuX-ZY.

	Cu-ZY	CuX-ZY	CuB-ZY
Reduction peaks: α / β / δ (°C)	351 / 439	334 / 494	456 / 501 / 654
Amount of H$_2$ gas adsorbed (μmol/g)	387.69	5074.34	5293.58
Metal surface (m^2/g$_{sample}$)	17.30	227.29	236.22
Dispersion degree (%)	12.32	61.82	68.18
Cu average particle diameter, d_{av}, (nm)	7.74	0.69	0.57

between 900 and 450 cm^{-1} regions of the spectrum which was assigned to asymmetrical T–O–T stretching and is indicative of heteroatom substitution [15,41,42]. This distortion is more pronounced in CuX-ZY with a new peak at 540 cm^{-1} ostensibly due to the substitution of dealuminated Al with highly downsized Cu^{2+}. The shift of the absorption bands at 1058 and 882 cm^{-1} further confirmed the incorporation of Cu^{2+} into the ZY lattice framework in CuX-ZY. Both Cu-ZY and CuB-ZY showed no observable shifts in those absorption bands and this is ascribed to their larger average Cu nanoparticles (relative to CuX-ZY according to the STEM-HAADF image in Fig. 2) that cannot gain access into the ZY lattice framework.

3.1.4. Reducibility patterns (H$_2$-TPR)

The TPR results of the three catalysts in Fig. 5 showed an asymmetrical spectra profile with instances of a shoulder and/or a tail that indicated the presence of a heterogeneous distribution of CuO species [7]. Typical reduction patterns for CuO to metallic state involve two stages: Cu^{2+} → Cu$^+$ (**peak α**) and Cu$^+$ → Cu^0 (**peak β**). The reduction temperatures (RT) for these peaks are shown in Table 3. The Cu-ZY sample has the lowest RT for peaks **α** and **β** at 351 and 439 °C, respectively, and these peaks shifted to higher temperatures in both CuB-ZY and CuX-ZY which indicated that the Cu species are having different types of interaction with the ZY support ostensibly due to variation in particle sizes. The values of **α** and **β** for the three catalysts are higher than what has been reported in most literature for supported unpromoted Cu systems for CO$_2$ hydrogenation. For example in a study of Cu supported on different ZrO$_2$ polymorphs; amorphous (-m), tetragonal (-t) and monoclinic (-m) phase, 201 and 232 °C were reported as the highest **α** and **β**, respectively for Cu/t-ZrO$_2$ [7]. Another catalyst system with Cu^{2+}: Zn^{2+}: Zr^{4+} = 6:3:1 synthesized by co-precipitation in the presence of NaBH$_4$ (as the in situ reducing agent) showed that the
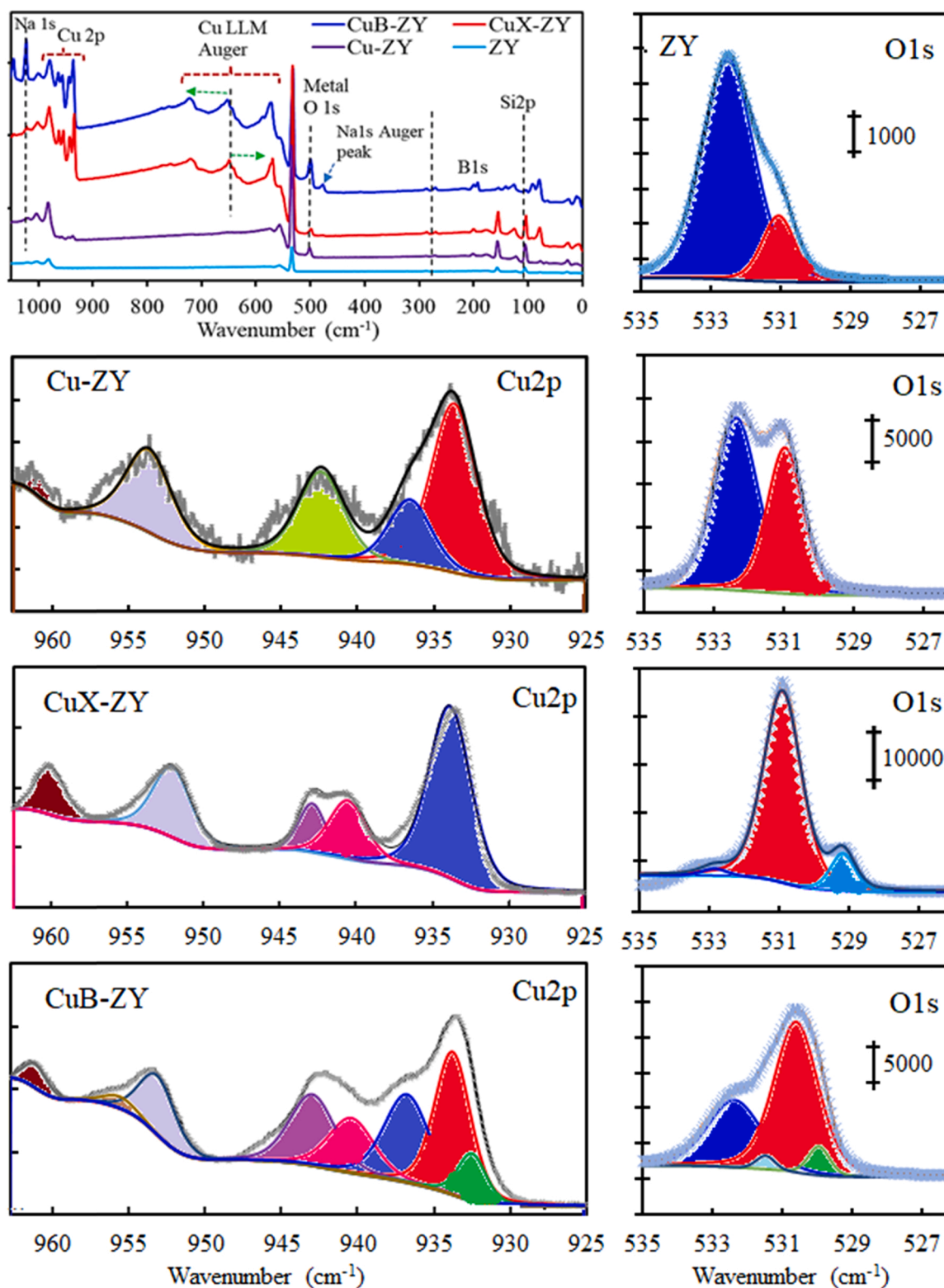
Fig. 6. XPS wide scan for ZY, Cu-ZY, CuX-ZY, and CuB-ZY and the Cu 2p and O 1 s narrow scan of the samples.

sample without NaBH$_4$ exhibited only one high RT peak γ at 196 °C which was attributed to the reduction of CuO [20]. Furthermore, as the amount of NaBH$_4$ increased, the RT peak γ disappeared while the peaks α and β progressively shifted to lower reduction temperatures.

In Fig. 5, the reduction peak α at 351 °C in Cu-ZY shifted slightly to lower temperature 334 °C in CuX-ZY possibly due to the presence of remnants of highly reducible Cu-OxA-ligands, while it appeared as peak $\acute{\alpha}$ at a significantly higher RT of 456 °C in CuB-ZY. The significant positive shift of peak $\acute{\alpha}$ relative to α is an indication of strong metal-support-interaction. The CuX-ZY showed peak β^1 at higher RT than β seen in the Cu-ZY sample. The peak β^1 can also be seen as a shoulder in the CuB-ZY. The shift of peak β^1 to higher RT further confirmed strong metal-support-interaction due to considerable downsizing of the Cu particle sizes according to the HRTEM image which is in close agreement

Table 4
Elemental and Cu oxidation ratios for samples.

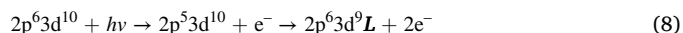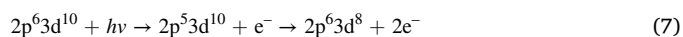|	O/Cu	Cu/O	Cu^+/Cu^{2+}	O_L/O_A
ZY	–	–	–	0.193
Cu-ZY	80.092	0.012	2.909	0.706
CuB-ZY	4.688	0.213	1.298	1.855
CuX-ZY	5.894	0.170	–	7.954

O_L/O_A = ratio of lattice oxygen to adsorbed oxygen.

with the H_2-TPD data in Table 3. Briefly, the TPD data showed that the Cu average particle diameter, d_{av}, in CuB-ZY and CuX-ZY are more than 11 times smaller than that of Cu-ZY leading to an increase in the Cu dispersion above 60% in those samples compared to the 12.3% in the Cu-ZY sample. Furthermore, it can be seen that the clear split of peaks α and β in the Cu-ZY tends to give way to a single feature in the CuX-ZY, and finally become a single $Cu^{2+} \rightarrow Cu^0$ peak in the CuB-ZY profile which connote the presence of ultra-low Cu particle size with a near-homogeneous particle size distribution in CuB-ZY (Table 3). This Cu particles size correlation with TPR RT observation is in agreement with another study involving a series of CuO/Al_2O_3-ZrO_2 catalysts prepared by sequential impregnation technique [43]. The study reported that as the Cu wt% decreased from 20% to 1.0%, the reduction peaks shifted to a higher temperature with the 1.0% Cu showing the highest RT peak at 389 °C. In addition, while two RT peaks α and β were observed at Cu loading 10% and above with both peaks shifted to lower RT as the Cu loading increased, only one reduction peak at higher RT was observed at Cu loading below 10% [43]. Moreover, the tail feature in the CuB-ZY sample is an indication of difficulty in reducing Cu oxides particles that are strongly interacting with the transformed ZY flowery morphology seen in the FESEM image. This is supported by the broad peak δ at 654 °C which indicated the reduction of low Cu contents and very small particle size within the micropore and/or diffusion of lattice oxygen to the surface [43]. Whereas, the lack of significant tail feature in the CuX-ZY catalyst suggested easy reduction possibly aided by the transformation of ZY support crystallinity into amorphous due to the OxA functionalization as seen in the XRD patterns. Thus, even though OxA and BH functionalization both achieved considerable Cu particle size reduction, it is evident that the Cu local structure, i.e., the coordination environment is different in both samples, as it will be further elucidated by the XPS results.

3.1.5. XPS - Surface chemistry and electronic properties

The results so far have confirmed significant morphological, structural, and heterogenous CuO reduction pattern responses to the OxA and BH functionalization, hence investigation of the surface chemistry and electronic structures of the samples with XPS becomes imperative. The XPS wide scan, the Cu 2p, and their O 1 s narrow scans of the samples are shown in Fig. 6. The Si, Al, and O presence can be seen in all the samples. The O 1 s peak due to the metal-oxygen bond can be seen at 535 eV in all the samples. A small peak at 191.08 eV and another one at ~497.5 eV in the CuB-ZY spectrum are due to the presence of boron from BH functionalization and the Na KLL line Auger peak, respectively. The incorporation of Cu from different precursors can also be seen with Cu reflection at ~935.08 eV. Both CuB-ZY and CuX-ZY showed the chemical shifts of the Cu LMM Auger lines which are considered to reflect the difference of the relaxation effect of the two-hole final state of Cu due to the electron donation ability of the surrounding constituents [44], i.e., $BH_4^-|Cu^{2+}|BH_4^-$ and $Cu^{2+}|C_2O_4^{2-}$ for CuB-ZY and CuX-ZY, respectively. The Cu-ZY sample does not show these Cu LMM Auger lines. To appreciate the origin of these Auger spectra, it is important to consider the Auger-electron emission process of Cu where the electron donation from ligand L to the metal ion (Cu) plays an important role in deciding the Auger-electron emission process.

In the case of Cu ions, the electron emission processes can be written as shown in Eqs. 7–8.

$$2p^6 3d^{10} + hv \rightarrow 2p^5 3d^{10} + e^- \rightarrow 2p^6 3d^8 + 2e^- \tag{7}$$

$$2p^6 3d^{10} + hv \rightarrow 2p^5 3d^{10} + e^- \rightarrow 2p^6 3d^9 \underline{\textbf{L}} + 2e^- \tag{8}$$

where $\underline{\textbf{L}}$ means a hole in the ligand $\textbf{L}$ of the first neighbor of the Cu ion [44]. To determine the kinetic energy of Auger electrons, the electron-donating capacity of the surrounding ligand becomes a significant factor. As seen in the O 1 s spectra of the samples, there are metal-oxygen bonds which implied that Cu ions are surrounded by oxygens (to a varying degree – see Table 4). Thus, the transition of an electron from the 2p orbital in oxide anions into a vacant Cu 2p orbital is the most dominant relaxation process containing ligands for the two-hole final state of Auger electron emission [44]. Furthermore, the difference in the coordination environment of Cu in the CuB and CuX samples explains the slight shift of the Cu LMM Auger lines toward lower BE in the latter (see XPS wide scan in Fig. 6 and Figure S2) due to the X-ray irradiation effects [44] and this agrees with the local Cu structures seen in the H_2-TPR profile results.

The Cu 2p narrow scan of the samples in Fig. 6 showed the presence of both Cu^+ and Cu^{2+} in Cu-ZY and CuB-ZY while CuX-ZY showed only Cu^{2+}. The presence of Cu^+ in Cu-ZY and CuB-ZY could be due to electron transfer arising from loss of framework/extra framework aluminum during catalyst synthesis and BH functionalization, respectively. Previous studies have demonstrated the capacity of $NaHB_4$ to initiate a series of reduction processes in Cu, i.e., $Cu^{2+} \rightarrow Cu^+ \rightarrow Cu^0$ [20]. The ratio of Cu^+/Cu^{2+} is higher in Cu-ZY than in CuB-ZY, which indicated smaller Cu particles sizes in the latter strongly interacting with the ZY support. The Cu $2p_{3/2}$ peaks of both Cu-ZY and CuB-ZY shifted to higher binding energy relative to the standard BE of 933.6 eV for bulk CuO which indicated a strong metal-support-interaction. This aligns with the H_2-TPR data with higher CuO reduction temperature peaks compared to those reported in the literature. There is a unique peak at BE ~0.6 eV lower than the typical BE of 933 eV for Cu^+ and Cu-metal in CuB-ZY. Such a low BE Cu 2p peak is very rare except in isolated cases such as Cu-molybdenite compounds ($Cu_2Mo_3O_{10}$ and $Cu_6Mo_4O_{15}$, Cu $2p_{3/2}$ = 932.2 eV) and Cu-ferrite spinel ($Cu_{1-x}Fe_{2+x}O_4$, Cu $2p_{3/2}$ = 931.3 eV) [44]. Accordingly, these low BE Cu peaks below the peak of Cu-metal in these compounds were ascribed to octahedral symmetry of the low BE Cu ions arising from the effect of the Madelung potential at the B-site in these compounds [44]. An anomalous behavior was observed in the Cu $2p_{3/2}$ of CuX-ZY which shifted slightly to lower BE due to X-ray irradiation effects. A similar anomalous chemical shift that induced the Cu 2p peak shifts towards the lower binding energy region until binding energy lower than that of metallic Cu has also been reported [44]. This X-ray irradiation effect further emphasizes the shift of the Cu LMM Auger lines toward lower BE (Figure S2) which has been ascribed to the difference in the coordination environment of Cu in CuB and CuX, and it is supported by the TPR profile. The possible presence of Cu-C bonding could also contribute to the Cu 2p peak shifts towards the lower binding energy (Figure S3).

The O 1 s spectra of the ZY support showed two peaks around ~532.8 eV and ~529.7 eV which are due to the adsorbed oxygen (O_A) and lattice oxygen, i.e., oxygen bonded to metal (O_L), respectively [8,18, 28]. The ratio of the O_L/O_A shown in Table 4 revealed that the ratio increased from 0.19 in the ZY support to 0.71 and 1.86 in Cu-ZY and CuB-ZY, respectively, while it drastically increased to 7.95 in CuX-ZY, which is consistent with previous reports on oxalate ligand functionalization [8]. The slight increase in Cu-ZY was due to the presence of O bonded to the supported Cu species. The further increase in the O_L/O_A in CuB-ZY was ascribed to the decrease in particle sizes of Cu. Ordinarily, O_L/O_A of CuB should be in the neighborhood of CuX based on their approximate Cu particles sizes according to the HRTEM and TPD desorption results, the significant difference was due to the presence of Cu-B bond which was shown in the Cu 2p of CuB-ZY at the BE ~932.8 eV, i.e., some of the Cu particles that could have been bonded to oxygen to increase the O_L were bonded to boron. The peak with BE
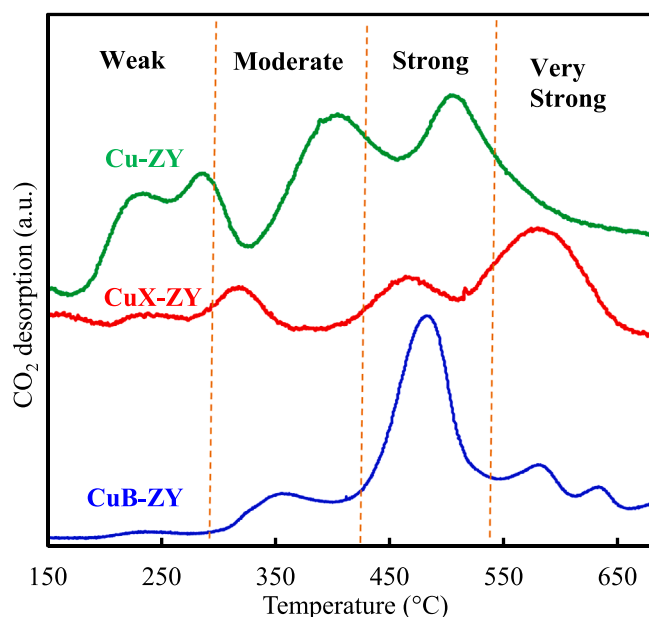
Fig. 7. TPD-CO_2 spectra for Cu-ZY, CuB-ZY, and CuX-ZY samples.

532.1 eV can be assigned to the O-B bond. The B 1 s narrow scan of the CuB-ZY is shown in Figure S4 with three distinctive features, a peak at 192.2 eV, a broad band with a peak at 187.7 eV, and another one at 182.1 eV. The peak at 192.2 eV is due to the B-O bond [45] earlier seen at BE 532.1 eV in the CuB-ZY O1s spectra, while the peak at 182.1 eV could be due to B-C arising from the presence of adventitious carbon and 187.7 eV due to B-Cu peak [46,47].

3.1.6. Basicity, TPD-CO_2

The difficulties associated with the activation of CO_2 have made its hydrogenation to methanol a challenging process, therefore, basic sites on the catalyst are essential to enhance the CO_2 adsorption for activation at the active sites. Thus, TPD-CO_2 was conducted to investigate the basicity of the samples. The samples were first reduced in a hydrogen environment based on the H_2-TPR information before CO_2 desorption studies to avoid interference of copper oxides phases on the true basicity of the samples. The Cu-ZY, CuB-ZY, and CuX-ZY samples showed heterogeneous basicity profiles in Fig. 7 which are due to different basic site strengths. Accordingly, the weak, moderate, and combined strong and very strong basic sites correspond to surface hydroxyl groups, metal-oxygen pairs (e.g., Cu-O and Al-O), and coordinatively unsaturated O^{2-} ions, i.e., low coordination oxygen atoms in the zeolite framework,

respectively [17,18,48]. Only Cu-ZY showed weak desorption peaks, while all three catalysts showed moderate and strong desorption peaks. Similarly, only CuB-ZY and CuX-ZY showed combined strong and very strong CO_2 desorption peaks. The quantification of all these peaks is presented in Table 5 which showed that the trend of the basic site followed CuB-ZY $>>$ CuX-ZY $>$ Cu-ZY. The presence of Na and BH_4^- are strongly responsible for the step increase in the basic sites of CuB-ZY. The absence of weak basic sites in both CuB-ZY and CuX-ZY was ascribed to the effect of BH_4^- and $C_2O_4^{2-}$ ligands functionalization at the synthesis stages that replaced their respective surface hydroxyl groups. Similarly, the highly downsized Cu particle sizes in both CuB-ZY and CuX-ZY contributed to their increased basicity, especially moderate and strong basic sites due to the increased metal-oxygen pairs and coordinatively unsaturated O^{2-} ions induced basicity [5]. These observations corroborate the findings in the FTIR spectra of the samples which showed a typical zeolitic broad band with a center around 3444 cm^{-1} due to structural acidity and another terminal Si-OH with inherent acidity at 882 cm^{-1} reduced significantly in CuB/ZY and CuX/ZY. In fact, the bridging Bronsted OH-groups with a more acidic hydroxyl band at 3624 cm^{-1} completely disappeared in these samples showing lesser acid sites that may impede the adsorption of the CO_2 species. Therefore, functionalization with OxA and BH leading to downsizing the Cu particles sized is essentially effective at reducing the acid sites and increasing the basic sites for CO_2 adsorption whilst also increasing the number of Cu active sites for CO_2 activation which indicates enhanced activity over both CuB-ZY and CuX-ZY [34].

3.2. Activity measurement

The CO_2 conversion (X_{CO2}) and the selectivity of identified products are shown in Fig. 8a-c. For the three catalysts, the X_{CO2} (Fig. 8a) increased at the reaction temperature increased from 180° to 270°C in accordance with reaction rates dependence on temperature, i.e., Arrhenius parameters within the allowable equilibrium conditions. Several parameters that may influence the CO_2 adsorption and activation such as total basic site density, β (Table 5); average Cu particle sizes, D_{av}; Cu dispersion, $\%D$; and exposed Cu sites, S_{Cu}, were fitted with the X_{CO2}, and they all showed strong correlation values, $R^2 > 0.99$ (Figure S5). Irrespective of the reaction temperature, the X_{CO2} followed the trend CuX-ZY $>$ CuB-ZY $>>$ Cu-ZY, i.e., the increase in X_{CO2} with an increase in reaction temperature is higher and closer in both CuB-ZY and CuX-ZY than Cu-ZY which indicated that the reduced acid sites, increased basic site, and highly downsized Cu particle sizes in both CuB-ZY and CuX-ZY were highly influential towards increasing the X_{CO2}. The apparent lower X_{CO2} response to an increase in temperature in Cu-ZY is significantly due to the larger Cu size (STEM-HAADF image in Fig. 2)

Table 5
(a) Total basic sites divided by the BET surface area in.

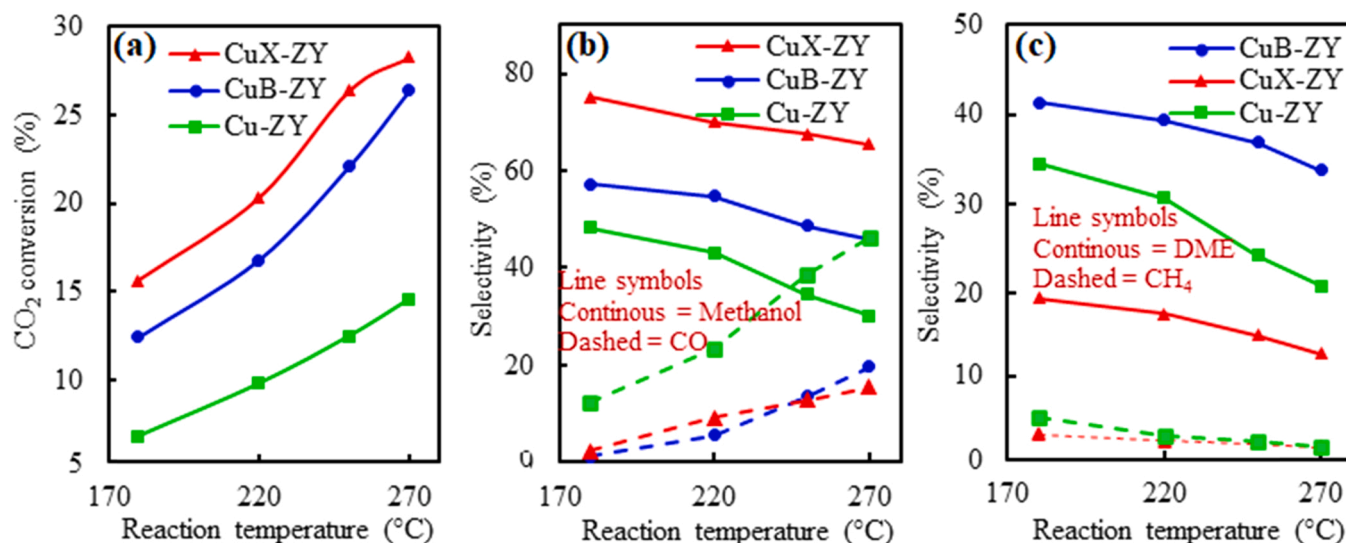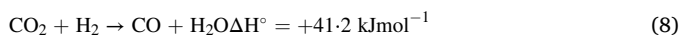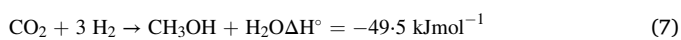| Sample	Peaks	Time to maximum desorption (min)	Desorption temperature (°C)	Amount of CO_2 desorption (μmol/g)	CO_2 desorption per peak (%)	[a]Total basic sites density (μmol/m^2)
Cu-ZY	1	11.7	285	14.5	15.8	
	2	12.9	310	12.5	13.6	
	3	18.4	411	25.4	27.7	
	4	22.8	503	39.4	42.9	
				$\Sigma = 91.8$		0.11
CuX-ZY	1	31.9	326	12.7	11.4	
	2	35.3	473	15.1	13.5	
	3	44.7	668	83.9	75.1	
				$\Sigma = 111.7$		1.10
CuB-ZY	1	16.1	356	51.5	11.9	
	2	22.5	482	279.3	64.5	
	3	27.5	580	72.4	16.7	
	4	30.2	633	30.0	6.9	
				$\Sigma = 433.2$		0.90

Fig. 8. (a) CO_2 conversion, (b) methanol and CO selectivity, (c) dimethyl ether and methane selectivity over Cu-ZY, CuX-ZY, and CuB-ZY catalysts.
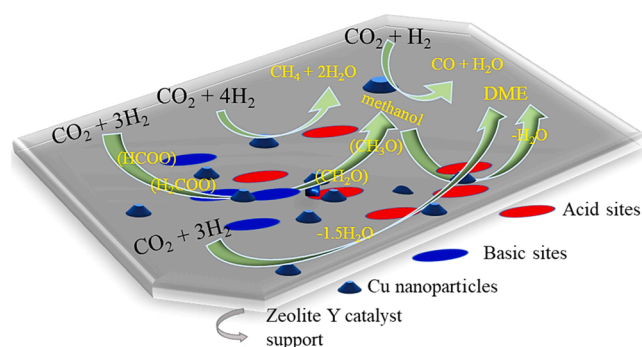
Scheme 1. CO_2 hydrogenation over smaller Cu nanoparticles to methanol while larger Cu nanoparticles favour conversion to CO. The acid sites favour dehydration of methanol to dimethyl ether (DME), while the basic sites prevent the formate decomposition to CO.

resulting in fewer Cu active sites (Table 3) which typically tend to favor CO formation, more so that methanol (MeOH) formation is thermodynamically limited at elevated temperature, Eqs. 7–8. In general, experimental and theoretical results have indicated extended surfaces of copper exhibit a low activity for CO_2 hydrogenation producing mainly CO with methanol as a minority product [1].

$$CO_2 + 3\,H_2 \rightarrow CH_3OH + H_2O\,\Delta H^\circ = -49.5 \text{ kJmol}^{-1} \qquad (7)$$

$$CO_2 + H_2 \rightarrow CO + H_2O\,\Delta H^\circ = +41.2 \text{ kJmol}^{-1} \qquad (8)$$

The product distribution showed that in addition to MeOH and CO, methane and dimethyl ether (DME) were also produced as summarized in Scheme 1. From Fig. 8b, the high MeOH selectivity (S_{MeOH}) over CuB-ZY and CuX-ZY compared to Cu-ZY was due to the impact of the BH and OxA ligands functionalization that respectively reconstructed the CuB-ZY and CuX-ZY textural, structural, acidic-basic properties, and introduce the XPS auger effect that confirmed the difference in the Cu local structures. The trend in the S_{MeOH} followed CuX-ZY > CuB-ZY > Cu-ZY which is consistent with the trend observed for the total basic site density, β (Table 5); average Cu particle sizes, d_{av}; Cu dispersion, $\%D$; and exposed Cu sites, S_{Cu}. Another important factor that could contribute significantly to the S_{MeOH} is the presence of Cu-C site arising from the decomposition of the oxalate ligand during calcination as seen in the C 1 s narrow scan at the usual metal carbide binding energy of ~283 eV (Figure S3). Metal carbides have been shown to display

interesting catalytic properties on their own in CO_2 hydrogenation. Depending on their carbon/copper ratio, they can adsorb CO_2 strongly and can cleave the C−O bonds in the molecule towards improving the S_{MeOH} by preventing the decomposition of formate to CO [1]. In addition, ultra-small Cu nanoparticle has active corner sites, i.e., defects induced reactive zones, and structural flexibility which acts to stabilize key intermediates (HCOO, H_2COO, and H_2CO) and reduces the barriers for hydrogenation, both of which also enhance the S_{MeOH} [49].

The CO selectivity, S_{CO}, was significantly low over CuX-ZY and CuB-ZY, i.e., < 20% at the highest reaction temperature of 270 °C, compared to 46.4% over Cu-ZY at the same temperature and even the S_{CO} range of 30–75% reported in the literature [1,5,7,20,48]. This implied that the strength between CO_2 and the CuX-ZY and CuB-ZY basic site is sufficiently strong to prevent the decomposition of formate to CO since it has been shown that CO is typically produced via the formate dissociation mechanism [7]. The S_{CO} increased with an increase in temperature because the reverse-water-gas-shift (RWGS) reaction is thermodynamically favored at high temperatures (Eq. 8). The trend in the S_{DME} in Fig. 8c followed CuB-ZY > Cu-ZY > CuX-ZY which is consistent with the trend observed for the pore structure in Fig. 2 and Table 1. This implied that both the secondary reaction of MeOH dehydration to DME (Eq. 9) and direct DME synthesis from CO_2-H_2 (Eq. 10) are favored by the large pore structure of CuB-ZY to accommodate the larger molecular size of DME. A previous study [6] has reported that CO_2 hydrogenation to oxygenates is structure and textural property sensitive, and the catalytic performance relies closely on the dimension and composition of the metal/metal oxide interface. Although acid sites are required for the DME synthesis chemistry, the higher S_{DME} over CuB-ZY than Cu-ZY implied that the enhanced pore structure and possibly the highly downsized Cu particle size effects are more significant. The lowest S_{DME} over CuX-ZY was ascribed to the combined effects of reduction and disappearance of Bronsted acidic characters at bands 3444 cm^{-1} and 3624 cm^{-1}, respectively, and even the significant reduction of the terminal acidic Si-OH groups at 882 cm^{-1}. Similarly, the near-collapse and drastic reduction of the micropore and mesopore structures, respectively arising from the considerable loss of the support zeolitic crystallinity structure in CuX-ZY according to the XRD patterns were also responsible for the lower S_{DME}.

Generally, in CO_2 hydrogenation chemistry, acid sites in zeolitic support materials are essential for the synthesis of DME, and altering the zeolite structure has been shown to alter product distributions and increase selectivity [22]. For example, HZSM-5 zeolite is selective towards DME [17] and gasoline, whereas SAPO molecular sieves are preferred
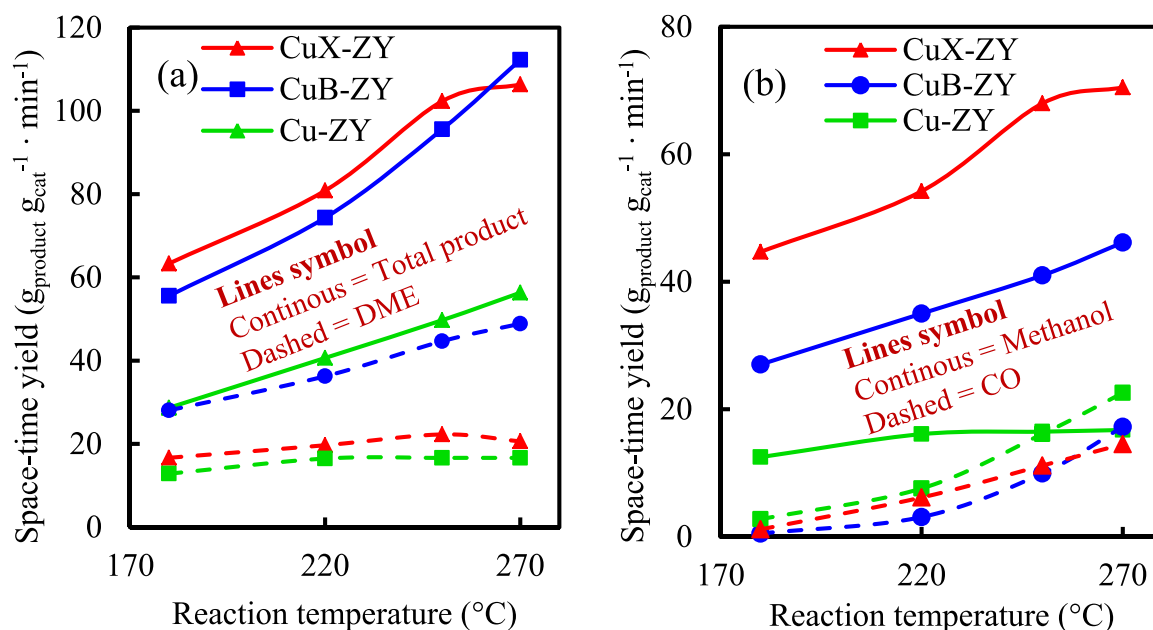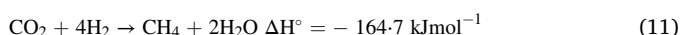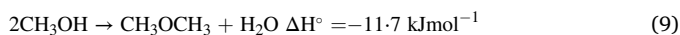
Fig. 9. Space-time-yield of products over Cu-ZY, CuX-ZY, and CuB-ZY.

for light olefin generation. [22]. Shape-selective catalysis was identified as a factor in these catalysts, as SAPO zeolite windows allowed only small linear hydrocarbons to pass, while H-ZSM zeolite windows allowed much larger branched and linear hydrocarbons to leave [22]. From Fig. 8c, in addition to the DME, there are instances of CH_4 formation over both Cu-ZY and CuX-ZY which is not observed over the CuB-ZY catalyst. In all cases, the DME and CH_4 selectivity reduced as the reaction temperatures increased, which is in tandem with the exothermicity of the reactions in Eqs. 9–11. To put the activity of the catalysts in perspective, the space-time yield for the total product ($\hat{Y}_{TP}$) and individual species ($\hat{Y}_i$) are plotted in Fig. 9a-b. Both $\hat{Y}_{TP}$ and $\hat{Y}_i$ for all the products increased monotonously with increase in reaction temperature in the order: CuX-ZY > CuB-ZY > > Cu-ZY corresponding to 102.3, 95.6, and 49.7 $g_{product} \, g_{cat}^{-1} \bullet min^{-1}$, respectively at 250 °C. As the reaction temperature was increased from 180° to 270°C, the increase in $\hat{Y}_{DME}$ was marginal ($< 5 \, g_{product} \, g_{cat}^{-1} \bullet min^{-1}$) over both CuX-ZY and Cu-ZY, while it significantly increase over CuB-ZY ($> 20 \, g_{product} \, g_{cat}^{-1} \bullet min^{-1}$) within the same temperature range. The influence of the combined enhanced pore structure and surface chemistry are effective for the synthesis of DME over CuB-ZY, as previously mentioned. The $\hat{Y}_{MeOH}$ over CuX-ZY and CuB-ZY also increased monotonously as the reaction temperature increased and reached the highest values of 70.5 and 46.2 $g_{product} \, g_{cat}^{-1} \bullet min^{-1}$ at 270 °C, while the $\hat{Y}_{MeOH}$ reached a maximum of 16.1 $g_{product} \, g_{cat}^{-1} \bullet min^{-1}$ over Cu-ZY at 220 °C and subsequently decreased with a consequent steep increase in the $\hat{Y}_{CO}$ as reaction temperature increased. As reaction temperature increased above 220 °C, the $\hat{Y}_{CO}$ is steeper over Cu-ZY compared to both CuX-ZY and CuB-ZY which confirmed that in addition to the endothermic nature of Eq. 8, the larger particles of Cu in Cu-ZY favoured CO formation.

$$2CH_3OH \rightarrow CH_3OCH_3 + H_2O \ \Delta H° = -11 \cdot 7 \ kJmol^{-1} \tag{9}$$

$$2CO_2 + 6H_2 \rightarrow CH_3OCH_3 + 3H_2O \ \Delta H° = -61 \ kJmol^{-1} \tag{10}$$

$$CO_2 + 4H_2 \rightarrow CH_4 + 2H_2O \ \Delta H° = -164 \cdot 7 \ kJmol^{-1} \tag{11}$$

4. Conclusions

The influence of oxalate and borohydride ligands functionalization on the property and activity of Cu supported on zeolite Y has been

systematically investigated in CO2 hydrogenation to methanol and dimethyl ether (DME). The synthesis protocol varied the properties of the catalyst which in turn impacted the final product selectivity. Both the CuX-ZY and CuB-ZY that underwent oxalate and borohydride ligands functionalization respectively exhibited a reduction in the acid sites, increase basic sites/strength, and produced highly downsized Cu average particles size for enhanced CO_2 adsorption and activation compared to a non functionalized Cu-ZY. The large Cu average particle sizes (APS) of 7.74 nm in Cu-ZY favored CO formation especially at the higher reaction temperature, while the low Cu APS of 0.57 and 0.69 nm for CuB-ZY and CuX-ZY, respectively favored methanol and DME. Furthermore, the results showed that large pores of CuB-ZY promoted the formation of DME, while the narrow pores of CuX-ZY favored methanol formation. The highest methanol and DME yields at the best reaction temperature of 270 °C are 70.5 $g_{product} \, g_{cat}^{-1} \bullet min^{-1}$ and 48.9 $g_{product} \, g_{cat}^{-1} \bullet min^{-1}$ over CuX-ZY and CuB-ZY, respectively. Thus, the oxalate and borohydride ligands functionalization protocol on CO2 hydrogenation catalysis is effective at minimizing unwanted CO formation and increasing selectivity to important industrial specialty chemicals – methanol and DME.

CRediT authorship contribution statement

The work is sole undertaken by the author.

Declaration of Competing Interest

The authors declare that they have no known competing financial interests or personal relationships that could have appeared to influence the work reported in this paper.

References

[1] J.A. Rodriguez, P. Liu, D.J. Stacchiola, S.D. Senanayake, M.G. White, J.G. Chen, Hydrogenation of CO2 to methanol: importance of metal−oxide and metal−carbide interfaces in the activation of CO_2, ACS Catal. 5 (2015) 6696–6706.
[2] H. Bahruji, M. Bowker, G. Hutchings, N. Dimitratos, P. Wells, E. Gibson, W. Jones, C. Brookes, D. Morgan, G. Lalev, Pd/ZnO catalysts for direct CO₂ hydrogenation to methanol, J. Catal. 343 (2016) 133–146.
[3] M. Behrens, F. Studt, I. Kasatkin, S. Kuhl, M. Havecker, F. Abild-Pedersen, S. Zander, F. Girgsdies, P. Kurr, B.L. Kniep, M. Tovar, R.W. Fischer, J.K. Norskov, R. Schlogl, The active site of methanol synthesis over Cu/ZnO/Al2O3 industrial catalysts, Science 336 (2012) 893–897.

[4] C.-L. Chiang, K.-S. Lin, H.-W. Chuang, Direct synthesis of formic acid via CO_2 hydrogenation over Cu/ZnO/Al2O3 catalyst, J. Clean. Prod. 172 (2018) 1957–1977.

[5] Y. Zhang, L. Zhong, H. Wang, P. Gao, X. Li, S. Xiao, G. Ding, W. Wei, Y. Sun, Catalytic performance of spray-dried Cu/ZnO/Al2O3/ZrO2 catalysts for slurry methanol synthesis from CO_2 hydrogenation, J. CO2 Util. 15 (2016) 72–82.

[6] X. Jiang, X. Nie, X. Guo, C. Song, J.G. Chen, Recent advances in carbon dioxide hydrogenation to methanol via heterogeneous catalysis, Chem. Rev. 120 (2020) 7984–8034.

[7] T. Witoon, J. Chalorngtham, P. Dumrongbunditkul, M. Chareonpanich, J. Limtrakul, CO_2 hydrogenation to methanol over Cu/ZrO2 catalysts: effects of zirconia phases, Chem. Eng. J. 293 (2016) 327–336.

[8] O.B. Ayodele, K.C. Lethesh, Z. Gholami, Y. Uemura, Effect of ethanedioic acid functionalization on Ni/Al2O3 catalytic hydrodeoxygenation and isomerization of octadec-9-enoic acid into biofuel: kinetics and Arrhenius parameters, J. Energy Chem. 25 (2016) 158–168.

[9] X.-F. Yang, A. Wang, B. Qiao, J. Li, J. Liu, T. Zhang, Single-atom catalysts: a new frontier in heterogeneous catalysis, Acc. Chem. Res. 46 (2013) 1740–1748.

[10] R. Jin, Y. Cao, C.A. Mirkin, K.L. Kelly, G.C. Schatz, J.G. Zheng, Photoinduced conversion of silver nanospheres to nanoprisms, Science 294 (2001) 1901.

[11] O. Ayodele, J. Lim, B. Hameed, Pillared montmorillonite supported ferric oxalate as heterogeneous photo-Fenton catalyst for degradation of amoxicillin, Appl. Catal. A: Gen. 413 (2012) 301–309.

[12] O.B. Ayodele, Effect of phosphoric acid treatment on kaolinite supported ferrioxalate catalyst for the degradation of amoxicillin in batch photo-Fenton process, Appl. Clay Sci. 72 (2013) 74–83.

[13] T. Margossian, K. Larmier, S.M. Kim, F. Krumeich, A. Fedorov, P. Chen, C. R. Müller, C. Copéret, Molecularly tailored nickel precursor and support yield a stable methane dry reforming catalyst with superior metal utilization, J. Am. Chem. Soc. 139 (2017) 6919–6927.

[14] Y. Wang, S. De, N. Yan, Rational control of nano-scale metal-catalysts for biomass conversion, Chem. Commun. 52 (2016) 6210–6224.

[15] O.B. Ayodele, W.M.A.W. Daud, Optimization of catalytic hydrodeoxygenation of oleic acid into biofuel using fluoroplatinum oxalate zeolite supported catalyst, J. Taiwan Inst. Chem. Eng. 47 (2015) 113–124.

[16] O.B. Ayodele, Structure and reactivity of ZSM-5 supported oxalate ligand functionalized nano-Fe catalyst for low temperature direct methane conversion to methanol, Energy Convers. Manag. 126 (2016) 537–547.

[17] O.B. Ayodele, Eliminating reverse water gas shift reaction in CO_2 hydrogenation to primary oxygenates over MFI-type zeolite supported Cu/ZnO nanocatalysts, J. CO2 Util. 20 (2017) 368–377.

[18] O.B. Ayodele, S.F.H. Tasfy, N.A.M. Zabidid, Y. Uemura, Co-synthesis of methanol and methyl formate from CO_2 hydrogenation over oxalate ligand functionalized ZSM-5 supported Cu/ZnO catalyst, J. CO2 Util. 17 (2017) 273–283.

[19] Y. Ma, Q. Sun, D. Wu, W.-H. Fan, Y.-L. Zhang, J.-F. Deng, A practical approach for the preparation of high activity Cu/ZnO/ZrO2 catalyst for methanol synthesis from CO_2 hydrogenation, Appl. Catal. A: Gen. 171 (1998) 45–55.

[20] X. Dong, F. Li, N. Zhao, F. Xiao, J. Wang, Y. Tan, CO_2 hydrogenation to methanol over Cu/ZnO/ZrO2 catalysts prepared by precipitation-reduction method, Appl. Catal. B: Environ. 191 (2016) 8–17.

[21] D. Jingfa, S. Qi, Z. Yulong, C. Songying, W. Dong, A novel process for preparation of a Cu/ZnO/Al2O3 ultrafine catalyst for methanol synthesis from CO_2 + H_2: comparison of various preparation methods, Appl. Catal. A: Gen. 139 (1996) 75–85.

[22] R.-P. Ye, J. Ding, W. Gong, M.D. Argyle, Q. Zhong, Y. Wang, C.K. Russell, Z. Xu, A. G. Russell, Q. Li, M. Fan, Y.-G. Yao, CO_2 hydrogenation to high-value products via heterogeneous catalysis, Nat. Commun. 10 (2019) 5698.

[23] P.L. Hansen, J.B. Wagner, S. Helveg, J.R. Rostrup-Nielsen, B.S. Clausen, H. Topsøe, Atom-resolved imaging of dynamic shape changes in supported copper nanocrystals, Science 295 (2002) 2053.

[24] Z. Liu, C. Shi, D. Wu, S. He, B. Ren, A simple method of preparation of high silica zeolite y and its performance in the catalytic cracking of cumene, J. Nanotechnol. 2016 (2016) 1486107.

[25] J. Wang, P. Liu, M. Boronat, P. Ferri, Z. Xu, P. Liu, B. Shen, Z. Wang, J. Yu, Organic-Free Synthesis of Zeolite Y with High Si/Al Ratios: Combined Strategy of In Situ Hydroxyl Radical Assistance and Post-Synthesis Treatment, Angew. Chem. Int. Ed. 59 (2020) 17225–17228.

[26] N. Katada, T. Takeguchi, T. Suzuki, T. Fukushima, K. Inagaki, S. Tokunaga, H. Shimada, K. Sato, Y. Oumi, T. Sano, K. Segawa, K. Nakai, H. Shoji, P. Wu, T. Tatsumi, T. Komatsu, T. Masuda, K. Domen, E. Yoda, J.N. Kondo, T. Okuhara, T. Kanai, M. Niwa, M. Ogura, M. Matsukata, E. Kikuchi, N. Okazaki, M. Takahashi, A. Tada, S. Tawada, Y. Kubota, Y. Sugi, Y. Higashio, M. Kamada, Y. Kioka,

K. Yamamoto, T. Shouji, S. Satokawa, Y. Arima, Y. Okamoto, H. Matsumoto, Standardization of catalyst preparation using reference catalyst: ion exchange of mordenite type zeolite: 2. Origin of dealumination and recommended standard conditions, Appl. Catal. A: Gen. 283 (2005) 75–84.

[27] D.-W. Zhuang, H.-B. Dai, P. Wang, Hydrogen generation from solvolysis of sodium borohydride in ethylene glycol–water mixtures over a wide range of temperature, RSC Adv. 3 (2013) 23810–23815.

[28] O.B. Ayodele, Influence of oxalate ligand functionalization on Co/ZSM-5 activity in Fischer Tropsch synthesis and hydrodeoxygenation of oleic acid into hydrocarbon fuels, Sci. Rep. 7 (2017) 10008.

[29] K.S.W. Sing, Reporting physisorption data for gas/solid systems with special reference to the determination of surface area and porosity (Recommendations 1984), Pure Appl. Chem. 57 (1985) 603–619.

[30] O.B. Ayodele, S.F.H. Tasfy, N.A.M. Zabidi, Y. Uemura, Co-synthesis of methanol and methyl formate from CO_2 hydrogenation over oxalate ligand functionalized ZSM-5 supported Cu/ZnO catalyst, J. CO2 Util. 17 (2017) 273–283.

[31] A.S. Kovo, O. Hernandez, S.M. Holmes, Synthesis and characterization of zeolite Y and ZSM-5 from Nigerian Ahoko Kaolin using a novel, lower temperature, metakaolinization technique, J. Mater. Chem. 19 (2009) 6207–6212.

[32] O. Ayodele, H.U. Farouk, J. Mohammed, Y. Uemura, W. Daud, Effect of precursor acidity on zeolite supported Pd catalyst properties and hydrodeoxygenation activity for the production of biofuel, J. Mol. Catal. A Chem. 400 (2015) 179–186.

[33] O.B. Ayodele, Physicochemical properties of acid/base activated kaolinite modified with oxalic acid-functionalized nickel nanoparticles, Catal. Today (2019).

[34] O.B. Ayodele, A.Z. Abdullah, Exploring kaolinite as dry methane reforming catalyst support: Influences of chemical activation, organic ligand functionalization and calcination temperature, Appl. Catal. A: Gen. 576 (2019) 20–31.

[35] D. Manyasree, P. Kiran Mayi, R. Ravikumar, CuO nanoparticles: synthesis, characterization and their bactericidal efficacy, Int. J. Appl. Pharm. 9 (2017).

[36] Y. Sun, P.A. Sermon, Evidence of a metal-support interaction in sol-gel derived Cu-ZrO2 catalysts for CO hydrogenation, Catal. Lett. 29 (1994) 361–369.

[37] H.G. Karge, Chapter 15 - characterization by IR spectroscopy, in: H. Robson, K. P. Lillerud (Eds.), Verified Syntheses of Zeolitic Materials, Elsevier Science, Amsterdam, 2001, pp. 69–71.

[38] Z. TVARUZKOVA, V. BOSACEK, Characterization of hydroxyl groups of Y zeolites by infrared spectra, J. Heyrovskij Inst. Phys. Chem. Electrochem. 29 (1975) 325–330.

[39] Z. Xie, X. Deng, X. Suo, T. Zhou, Y. Gou, Synthesis and characterization of zirconium diboride precursor based on polycentric bridge bonds, Mater. Chem. Phys. 159 (2015) 178–184.

[40] S. Das, A. Bedar, A. Kannan, K. Jasuja, Aqueous dispersions of few-layer-thick chemically modified magnesium diboride nanosheets by ultrasonication assisted exfoliation, Sci. Rep. 5 (2015) 10522.

[41] A. Nezamzadeh-Ejhieh, Z. Shams-Ghahfarokhi, Photodegradation of methyl green by nickel-dimethylglyoxime/ZSM-5 zeolite as a heterogeneous catalyst, J. Chem. (2013) () (2012).

[42] O. Ayodele, O. Togunwa, Catalytic activity of synthesized bentonite supported cuprospinel oxalate catalyst on the degradation and mineralization kinetics of Direct Blue 71, Acid Green 25 and Reactive Blue 4 pollutants in photo-Fenton process, Appl. Catal. A 470 (2014) 285–293.

[43] G.V. Sagar, P.V.R. Rao, C.S. Srikanth, K.V.R. Chary, Dispersion and reactivity of copper catalysts supported on Al2O3−ZrO2, J. Phys. Chem. B 110 (2006) 13881–13888.

[44] T. Yano, M. Ebizuka, S. Shibata, M. Yamane, Anomalous chemical shifts of Cu 2p and Cu LMM Auger spectra of silicate glasses, J. Electron Spectrosc. Relat. Phenom., 131- 132 (2003) 133–144.

[45] X. Liu, X. Chen, D.J. Singh, R.A. Stern, J. Wu, S. Petitgirard, C.R. Bina, S. D. Jacobsen, Boron–oxygen complex yields n-type surface layer in semiconducting diamond, Proc. Natl. Acad. Sci. 116 (2019) 7703.

[46] V. Harnchana, A.T. Hindmarch, M.C. Sarahan, C.H. Marrows, A.P. Brown, R.M. D. Brydson, Evidence for boron diffusion into sub-stoichiometric MgO (001) barriers in CoFeB/MgO-based magnetic tunnel junctions, J. Appl. Phys. 113 (2013), 163502.

[47] P. Malinovskis, J. Palisaitis, P.O.Å. Persson, E. Lewin, U. Jansson, Synthesis and characterization of MoB2−x thin films grown by nonreactive DC magnetron sputtering, J. Vac. Sci. Technol. A 34 (2016), 031511.

[48] C. Huang, S. Chen, X. Fei, D. Liu, Y. Zhang, Catalytic hydrogenation of CO_2 to methanol: study of synergistic effect on adsorption properties of CO_2 and H2 in CuO/ZnO/ZrO2 System, Catalysts 5 (2015).

[49] Y. Yang, J. Evans, J.A. Rodriguez, M.G. White, P. Liu, Fundamental studies of methanol synthesis from CO_2 hydrogenation on Cu(111), Cu clusters, and Cu/ZnO (000⁻), Phys. Chem. Chem. Phys. 12 (2010) 9909–9917.